Anti-reflection coating of laser-ablated sub-wavelength structure for millimeter-wave alumina filters

Kosuke Aizawa[a], Ryosuke Akizawa[a], Scott Cray[b], Shaul Hanany[b], Jürgen Koch[c], Kuniaki Konishi[d], Tomotake Matsumura[e,f,g], Haruyuki Sakurai[d], and Ryota Takaku[e,h]

[a]Department of Physics, The University of Tokyo, 7-3-1 Hongo, Bunkyo-ku, Tokyo 113-8654, Japan
[b]School of Physics and Astronomy, University of Minnesota, Twin Cities, 115 Union St. SE, Minneapolis MN 55455, USA
[c]Laser Zentrum Hannover, Hollerithallee 8 D-30419, Hannover, Germany
[d]Institute for Photon Science and Technology (IPST), The University of Tokyo, 7-3-1 Hongo, Bunkyo-ku, Tokyo 113-8654, Japan
[e]Kavli Institute for the Physics and Mathematics of the Universe (IPMU), The University of Tokyo, 5-1-5 Kashiwa-no-Ha, Kashiwa, Chiba 277-8583, Japan
[f]Center for Data Driven Discovery (CD3), Kavli Institute for the Physics and Mathematics of the Universe (IPMU), The University of Tokyo, 5-1-5 Kashiwa-no-Ha, Kashiwa, Chiba 277-8583, Japan
[g]ILANCE, CNRS, University of Tokyo International Research Laboratory, Kashiwa, Chiba 277-8582, Japan
[h]Inter-University Research Institute Cooperation High Accelerator Research Organization (KEK) International Center for Quantum-field Measurement Systems for Studies of the Universe and Particles (QUP), 1-1, Oho, Tsukuba, Ibaraki, 305-0801, Japan

ABSTRACT

We present designs and fabrications of sub-wavelength anti-reflection structures on alumina for infrared filters at three observational frequency bands near 30, 125, and 250 GHz, which are widely used for instruments measuring cosmic microwave background (CMB) radiation from the ground. The three observational windows contain the two observational bands in each receiver, and the corresponding fractional bandwidth is about 60%. We used laser ablation to directly machine on alumina substrate. This technology is robust against the use of an optical element at the cryogenic temperature with which all the CMB telescope receivers have to comply. Based on the fabricated 9 (3×3) pyramidal structures, we computed the expected averaged transmittance of above 0.97 for each of the three filter designs including anticipated absorptive loss, the loss tangent of 4×10^{-4}, and the incident angle up to 20 degrees. The band averaged instrumental polarization, the fractional difference between the p and s-state incident polarization states, is computed and they are less than $\pm 4 \times 10^{-3}$ for the bands and incident angles.

Keywords: IR absorption filter, anti-reflection coating, sub-wavelength structures, laser machining, cosmic microwave background

1. INTRODUCTION

Cosmic inflation provides solutions to several otherwise unresolved questions in modern cosmology. If inflation exists, it leaves a B-mode pattern in the cosmic microwave background polarization.[1,2] The level of the B-mode amplitude can be related to the energy scale of inflation with the parameter, the tensor-to-scalar ratio r,

Further author information:
K. Aizawa: E-mail: kosuke.aizawa@ipmu.jp, Tel (IPMU): +81 04 7136 4940

Millimeter, Submillimeter, and Far-Infrared Detectors and Instrumentation for Astronomy XII,
edited by Jonas Zmuidzinas, Jian-Rong Gao, Proc. of SPIE Vol. 13102,
131021Z · © 2024 SPIE · 0277-786X · doi: 10.1117/12.3018686

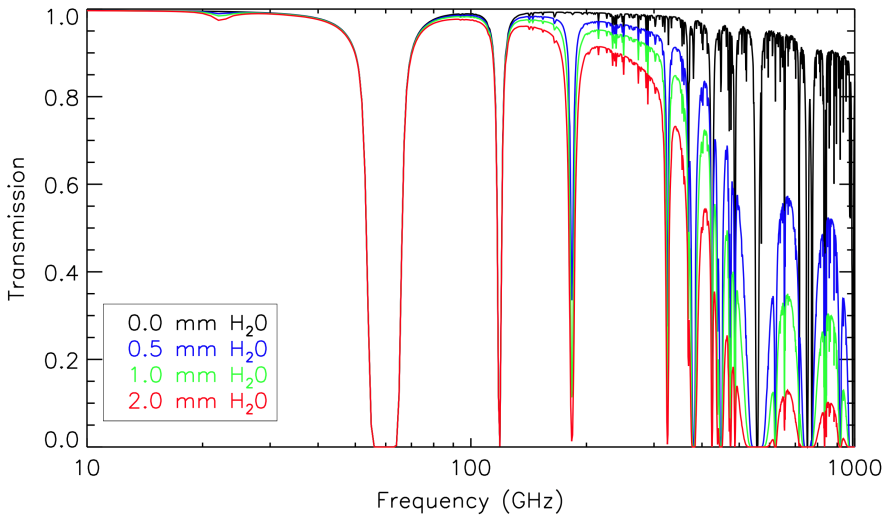

Figure 1. The atmospheric transmission at Atacama, Chile. The figure is taken from Errard et al.[25]

and many CMB polarization experiments aim to constrain this signal at levels $r \sim 10^{-3}$ in a coming decade. To achieve the required sensitivity, an observational cryogenic receiver has to be facilitated to achieve large throughput with $\sim 10^{5-6}$ superconducting detector arrays maintained at $0.1 \sim 0.3$ K.

As the desired sensitivity becomes higher, the experimental challenges associated with cryogenics become stringent.[3] One of the key challenges is to increase the throughput of a cryogenic receiver for millimeter-wave while we ensure to block infrared (IR) radiation through the cryostat window in order to minimize heat input. As a result, any CMB receivers employ an IR blocking filter, e.g. metal-mesh based infrared reflective filter.[4] A large throughput receiver leads to a large diameter optical element, and the optical elements made of any low thermally conductive material, e.g. plastic, add the challenge to cool the central portion of the optical element with respect to the thermally sunk edge, or otherwise the optical element itself becomes a source of the thermal emission.

Alumina, aluminum oxide, is a dielectric material that has the thermal conductivity of $\sim 10^3$ W/m·K at 100 K,[5] the loss-tangent of $\sim 10^{-4}$, and the index of refraction of about 3.[6] Alumina is proposed to be the base material of the IR absorptive filter.[7,8] Despite the attractive material properties in alumina, the anti-reflection coating has to be applied robustly for use at cryogenic temperatures. Takaku et al. demonstrated the fabrication of the IR absorptive filter using the sub-wavelength structure (SWS) based anti-reflection (AR) using the laser ablation on both surfaces.[8] This was focused on the bandwidth between 75 and 105 GHz, and became the first on-sky optical elements using the laser-machined AR-SWS for the MUSTANG-2 receiver on Green Bank Telescope.

The successful implementation of the AR SWS using the laser together with the development heritage brings to the next step, a broader bandwidth on a polarization-sensitive telescope.[9–17] Due to water and oxygen lines of the atmosphere, the typical CMB polarization telescopes have an atmospheric window of around 30, 125, and 250 GHz (see Fig. 1.) In this paper, we design the AR coating using SWS for IR filters optimized for three typical atmospheric windows of a ground-based millimeter-wave telescope, specifically for the CMB polarization experiments.[18–24] The paper is structured as IR filter design (Section 2), prototype fabrication of the AR-SWS (Section 3), estimated transmittance of the prototype (Section 4), and forecast of the optical performance (Section 5).

2. DESIGN

We designed three types of alumina filters matching the frequency bands of the typical CMB ground telescopes as summarized in Table 1. In this paper, we chose the observational bands for SO-SAT as a case study, but the

Table 1. The list of the ongoing and upcoming ground-based CMB polarization experiments and their observational bands. Three types of telescope receivers, labeled as Low Frequency (LF), Middle Frequency (MF), and High Frequency (HF), have two observational bands in each telescope. Each experiment has a telescope that covers two observational The first row of each experiment is the center frequency (unit: GHz), and the second row is the fractional bandwidth.

CMB exp.	Low Frequency	Middle Frequency	High Frequency
BICEP/Keck[18]	30, 40	95, 150	220, 270
	0.25, 0.25	0.25, 0.25	0.25, 0.25
SPTpol[19]	-	90, 150	-
	-		-
Ali-CPT[20]	-	91.4, 145	-
	-	0.4, 0.3	-
SimonsArray/POLARBAER-2[21]	-	89.5, 147.5	220, 280
	-	0.324, 0.260	
SO (SAT)[22]	27, 39	93, 145	225, 280
	0.3, 0.3	0.3, 0.3	0.3, 0.3
SO (LAT)[24]	27, 39	93, 145	225, 280
CMB-S4 (SAT)[23]	26, 39	85, 145 (MF1) / 95, 155 (MF2)	227, 286
	0.33, 0.45	0.24, 0.22 / 0.24, 0.22	0.26, 0.21
CMB-S4 (LAT)[23]	20 (ULF) / 26, 39 (LF)	92, 149	227, 286
	0.25 / 0.33, 0.45	0.32, 0.28	0.26, 0.21

results do not strongly depend on this choice due to the proximity of the specifications. The key construction parameters are the AR-SWS shape (see Figure 2), the thickness of the filter itself, and the material properties of alumina: the index of refraction and the loss-tangent. We used the index of alumina to be $n = 3.12$ and $\tan\delta = 4 \times 10^{-4}$.[8] The thickness of the alumina without accounting for the thickness of SWS-AR is chosen to be 2.4 mm. This is the same as the thickness chosen in MUSTANG-2 alumina filter. We are aware of the tradeoff in the choice of this thickness for the absorption in the millimeter-wave observational band and in the THz and IR bands. Also, this plate needs to be rigid enough for machining, handling, and potential stress due to thermal contraction. The optimal choice in this tradeoff may be different depending on the target experiment. Therefore, we leave this optimization as a future study for specific applications and employ the thickness from the successful implementation in MUSTANG-2 in this paper.

The optimization step is the following. Each telescope has two central observational frequencies, ν_{cl} and ν_{ch}, with the fractional bandwidth of $\Delta\nu/\nu_{cl}$ and $\Delta\nu/\nu_{ch}$. We take the highest observational band edge in the

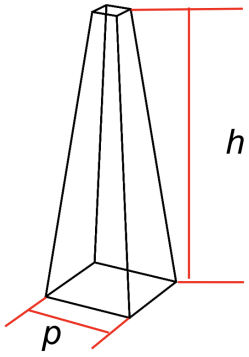

Figure 2. The definition of geometric parameters of motheye structure that are changeable in the process of design optimization. Note that while Γ_m is not a implicit geometric parameter in the structure, varying Γ_m gives minor changes of both geometric structure of motheyes including the curvature of taper and width of the top of structures.

Table 2. The averaged transmittance at each band is calculated by using two methods: second-order EMT and RCWA assuming a top-hat band shape with taking into account the loss being $\tan\delta = 4\times10^{-4}$.

$(\tan\delta = 4\times10^{-4})$	LF		MF		HF	
Frequency band [GHz]	27	39	93	145	225	280
EMT	0.970	0.988	0.971	0.980	0.971	0.970
RCWA	0.982	0.987	0.977	0.983	0.967	0.974

Table 3. The parameters used for the laser machining.

Model: Carbide CB3	
Maximum power	40 W
Wavelength	1030 nm
Repetition rate	100 kHz
Pulse duration	4 ps
Spot diameter $(1/e^2)$	30 μm

telescope, $\nu_h = \nu_{ch}(1 + 0.5\Delta\nu/\nu_{ch})$. The pitch of the AR SWS, p, (see Figure 2) is determined by

$$p \leq \frac{c/\nu_h}{n_a + \sin\theta_i}, \tag{1}$$

where c is the speed of light, n_a is the index of alumina, and θ_i is the incident angle of the incoming radiation with respect to the alumina filter based on the field-of-view. We assumed $\theta_i = 17.5$ degrees, which we refer to the SO field-of-view for a case study.[26] As a result, we computed the pitch to be 1.95, 0.52, and 0.27 mm for Low Frequency band (LF), Middle Frequency band (MF), and High Frequency band (HF), respectively.

The optimal index profile for broadband frequency coverage has been investigated by Klopfenstein.[27] We parameterize the index profile with two parameters, the height h and the profile parameter Γ_m. We then use the second-order effective medium theory (EMT) to relate the linear fill fraction to the effective index at a given height. In this way, we can compute the effective indices as a function of height with the resolution of 200 layers, and further compute the transmittance from the SWS shape by replacing the stack of multilayer films using the transfer matrix method (TMM).[28] We repeat this calculation for the given h and Γ_m. The first row of Figure 3 shows the band averaged transmittance, $\bar{T}_l$ and $\bar{T}_h$, for two sub-bands in each frequency band. Note that this transmittance takes into account the loss as $\tan\delta = 4\times10^{-4}$. Then, we picked up the minimum value of h which satisfies both $\bar{T}_l$ and $\bar{T}_h$ being greater than 0.97 simultaneously. The averaged transmittance 0.97 is set as a threshold value for design guidance in each frequency band. This threshold can be set higher or lower depending on the application, and this choice is not limited by this optimization method. After fixing the value of h, we extracted corresponding Γ_m where both $\bar{T}_l$ and $\bar{T}_h$ are greater than 0.97 again.

The second row of Figure 3 shows the resultant SWS profile for LF, MF, and HF on the left panel, and the index profile on the right panel. Finally, the third row shows the transmittance of the optimized geometry computed by the second order EMT and TMM and also Rigorous Coupled Wave Analysis (RCWA) based commercial software* We specifically use the combination of the second-order EMT and TMM for this optimization due to the advantage of the computational speed as compared to the RCWA even though the second-order EMT is based on an approximated method. Because of this reason, we computed the transmittance of the selected geometry using RCWA to ensure that the performance is high enough. The averaged transmittance after the optimization is summarized in Table 2. Note that the exact averaged transmittance depends on the detailed shape of the fringe pattern, which is affected by both the SWS shape and the thickness of the native sample, 2.4 mm in our case study. Thus, we should keep in mind this extra parameter space for further optimization.

3. FABRICATION

The 3×3 SWS array is fabricated on an alumina plate† following the designed shape using laser machining. The detailed laser parameters are listed in Table 3.

*diffractMOD by Synopsys, Inc.

†99.5LD, CERATEC CO., LTD.

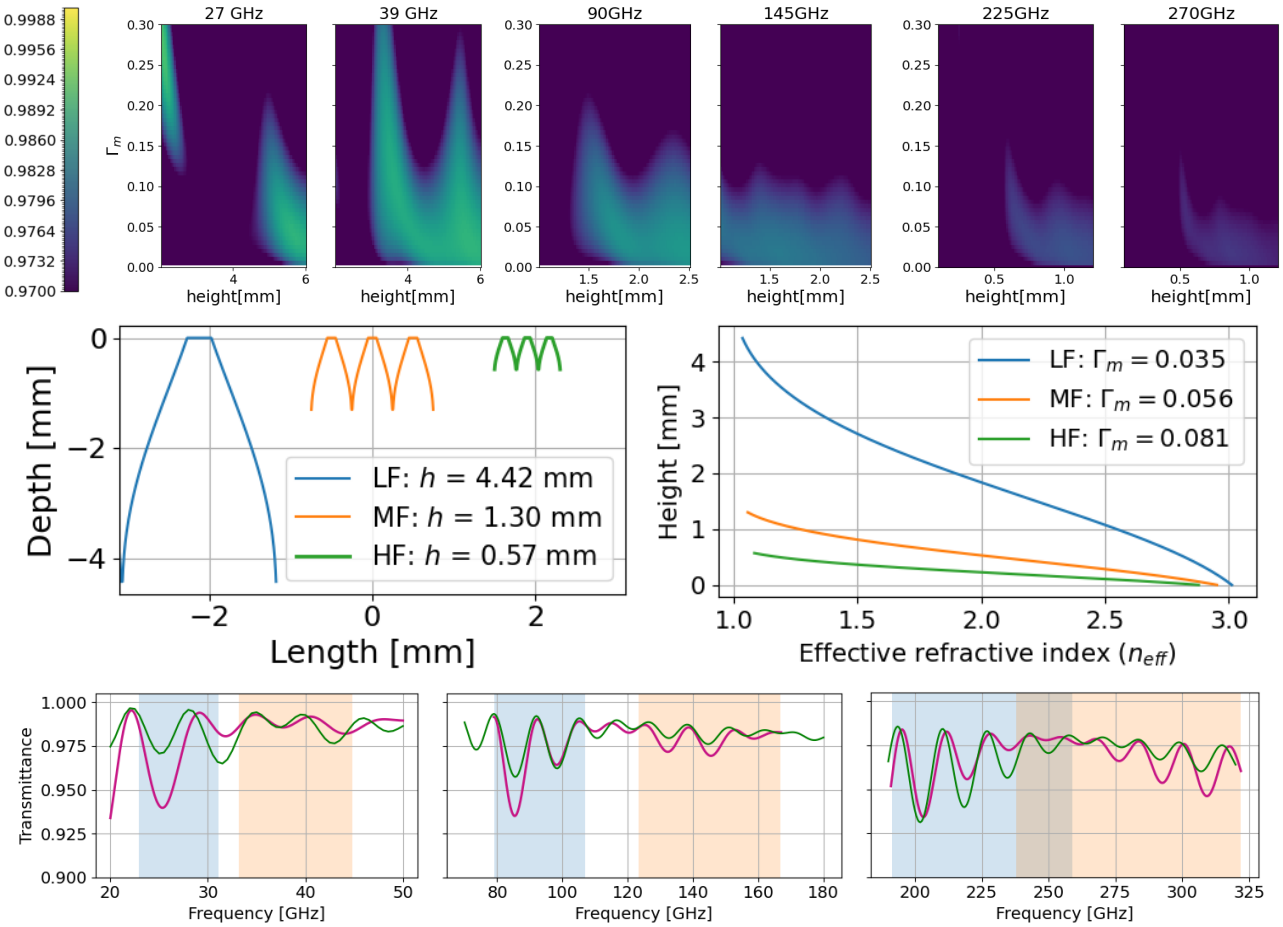

Figure 3. The averaged transmittances as a function of height (h) and Γ_m in the first row. The SWS profile of the calculation under specific h and Γ_m extracted from the calculations in the first row is on the left of the second row and the index profile is on the right. Extracted values of h and Γ_m are shown in the legend box of the figure for the SWS profile and the one for the index profile, respectively. The transmittance spectrum from which we obtained the band average transmittance as the design for each frequency band is shown in the third row. The three columns are for LF, MF, and HF, respectively. We show the ones calculated by two types of calculation methods: the second-order EMT (red) and the RCWA-based calculation (green).

The left side of Figure 4 shows 3D plots of the surface of the fabricated structures measured by the confocal microscope[‡]. On the right panel, the orientations along which each definition of depth is measured is given as dashed arrows. Only the structure for LF is shown as an example to indicate what fabricated structures look like. Figure 6 shows the cross-sectional view of the fabricated shape and the designed shape. Also, the derived index profile from the fabricated structure using the second-order EMT is shown in Figure 7. We further characterized the shape parameters as summarized in Table 4.

4. RESULTS

We have computed the prospective performance in transmittance by constructing the IR filter model. The IR model consists of the pyramidal structure applied on both sides of the base alumina. As shown in Figure 6, the pyramidal shapes are not identical in x and y directions. When the two pyramids are placed on both sides of the alumina, we rotates one side of the pyramid by 90 degrees with respect to the other side of the pyramid to symmetrize, as we have demonstrated its effectiveness in Takaku et al.[8] The pyramid is taken from the center

[‡]KEYENCE, VK-X1000

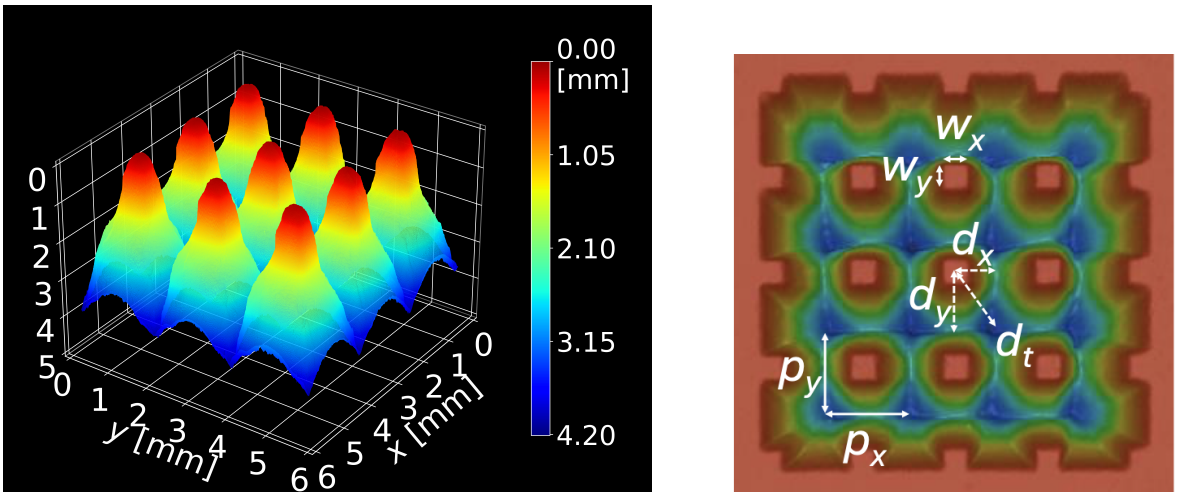

Figure 4. Left: 3D image of 3 × 3 SWS for LF fabricated by the laser machining. The structures are scanned by the confocal microscope. Right: The orientations along which each definition of depth is measured are shown as dashed arrows.

Table 4. The averaged shape parameters from the nine pyramids are listed for each frequency band. Errors in each row is the standard deviation of parameters of nine motheyes on each sample.

Shape parameters [mm]	LF	MF	HF
Saddle depth x (d_x)	3.22 ± 0.01	0.89 ± 0.003	0.45 ± 0.02
Saddle depth y (d_y)	3.20 ± 0.04	0.92 ± 0.02	0.39 ± 0.01
Total depth (d_t)	4.13 ± 0.07	1.33 ± 0.01	0.66 ± 0.01
Top width x (w_x)	0.43 ± 0.03	0.14 ± 0.01	0.06 ± 0.004
Top width y (w_y)	0.42 ± 0.03	0.15 ± 0.01	0.05 ± 0.003

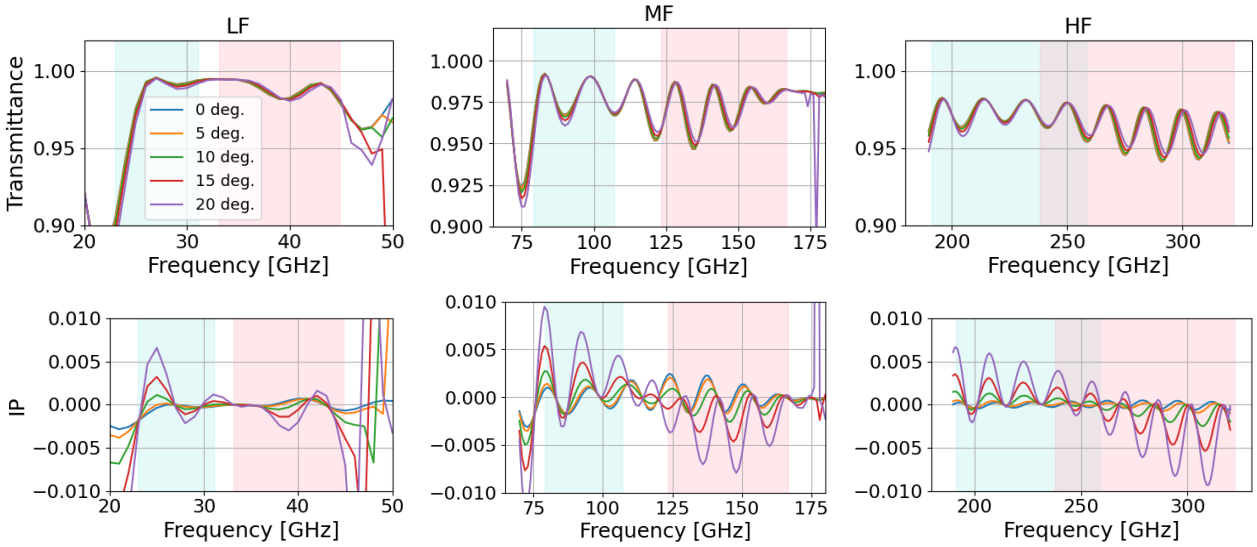

Figure 5. Predicted transmittance of incident light of p-polarized state and s-polarized state using RCWA and subsequently calculated IP for each frequency band varying incident angle 0°, 5°, 10°, 15°, 20°. The calculations are made under the assumption that SWS is fabricated on both sides of the alumina plate and one is rotated by 90° about the vertical axis, and the thickness of the substrate between two coating layers is 2.4 mm.

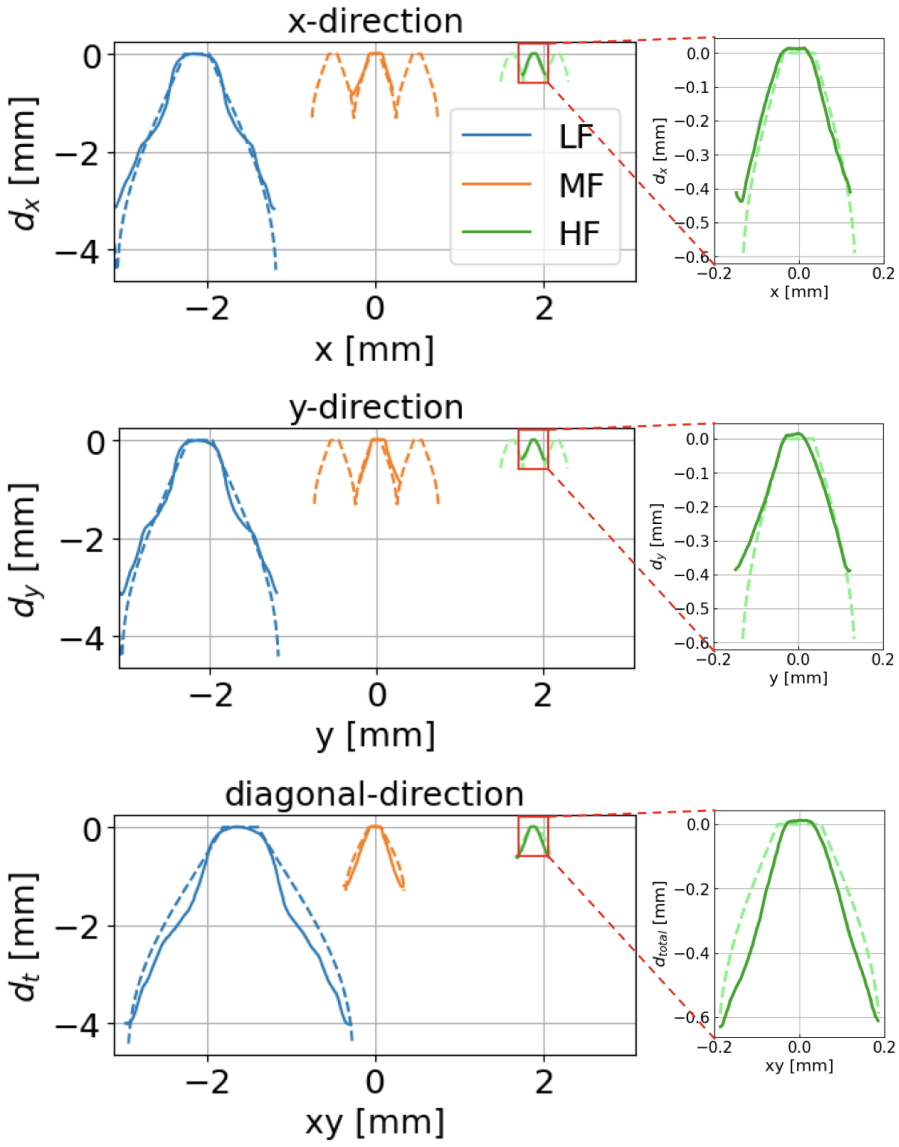

Figure 6. Overlap of cross-sectional view of the fabricated shape (solid line) for each direction; x direction, y direction, and diagonal direction over the designed shape (dashed line). Cross-sectional view of the fabricated shape is average of cross-sectional data of all nine pyramids.

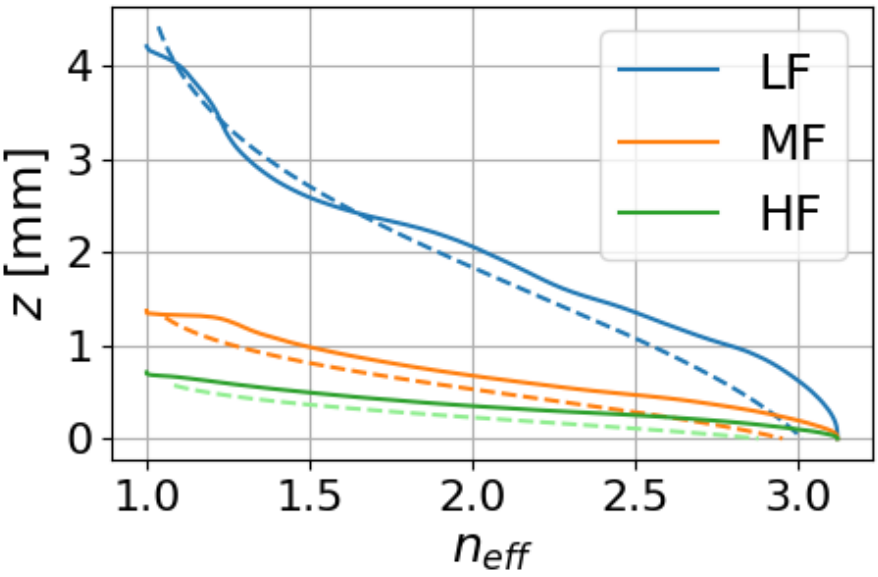

Figure 7. Overlap of index profile of the fabricated shape (solid line) and Klopfenstein-based design (dashed line) for each three frequency band.

Table 5. List of the averaged transmittance and the instrumental polarization for each incident angle.

		Frequency band [GHz]					
		LF		MF		HF	
	Incident angle	27	39	93	145	225	280
$\bar{T}$	$\theta_i = 0°$	0.976	0.989	0.980	0.973	0.973	0.963
	$\theta_i = 5°$	0.976	0.989	0.980	0.973	0.973	0.963
	$\theta_i = 10°$	0.975	0.989	0.980	0.973	0.973	0.963
	$\theta_i = 15°$	0.973	0.989	0.979	0.973	0.972	0.964
	$\theta_i = 20°$	0.970	0.989	0.978	0.973	0.972	0.965
$I\bar{P}$	$\theta_i = 0°$	0.000	0.000	0.000	0.000	0.000	0.000
	$\theta_i = 5°$	0.000	0.000	0.000	0.000	0.000	0.000
	$\theta_i = 10°$	0.000	0.000	0.000	-0.001	0.001	0.001
	$\theta_i = 15°$	0.000	0.000	0.001	-0.002	0.001	0.002
	$\theta_i = 20°$	0.001	-0.001	0.003	-0.003	0.003	0.004

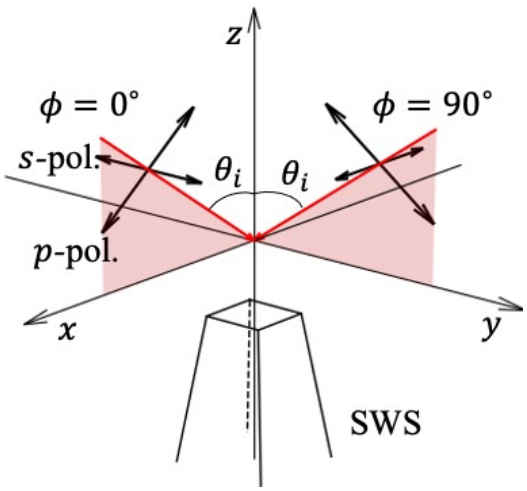

Figure 8. The schematic image of incident angle and polarization.[29] ϕ is the rotational angle of incident light about z axis of SWS. θ_i is the incident angle, and translucent red areas on xz plane and yz plane indicate the incident planes at each ϕ.

of the 3×3 SWS array as a representative SWS. The base alumina thickness is chosen to be 2.4 mm. This is one of the optimization parameters when an IR filter designer optimizes for specific applications.

Figure 5 shows the RCWA based predicted transmittance spectrum for five different incident angles over the relevant frequency range using the diffractMOD. We also compute the instrument parameter called "instrumental polarization (IP)", the measure of the conversion fraction from the unpolarized light to the polarized light as

$$IP(\nu) = \frac{T_S(\nu) - T_P(\nu)}{T_S(\nu) + T_P(\nu)}, \tag{2}$$

where T_P and T_S are transmittance of p-polarized and s-polarized incident light, respectively. The polarization direction of p-polarized state and s-polarized state are defined in Figure 8. Predicted optical performance in band average transmittance and band average of IP for each of two sub-band in each frequency band is shown in Table 5.

5. DISCUSSIONS

The focus of this paper was the demonstration of the design procedure, the design and fabrication feasibility, and the simulation-based forecast of the transmittance and instrument polarization based on the fabricated structures. Due to the faster iteration process, we made only the small SWS array as shown in Figure 4. This may leave a question of the uniformity over the larger surface area, thus we fabricated the AR SWS for MF on the alumina disk over the diameter of 60 mm, and characterized the variation of the shape parameters within this area. Note that the eventual goal for this technology is to be applied to even larger diameter, > 0.5 m which is beyond the scope of this paper, and leave that to future studies.

Figure 9 shows the fabricated area of AR SWS array and the locations where the conformal microscope images were taken. The five locations, area 1 (center), area 2 (north), area 3 (east), area 4 (south), and area 5 (west), contain about 1300, 1100, 600, 800, and 500 pyramids, respectively. We extracted the geometrical parameters of the saddle height in x and y and the total height as average of motheyes in each of five areas shown in Table 6 with standard deviations. Figure 10 shows the histograms of the parameters from all pyramids of five areas. The distribution is consistent with the normal distribution. We extracted the mean and the sigma by fitting the Gaussian shape, and the fitted parameters are summarized in Table 7. The 1σ variation is within 1-2%.

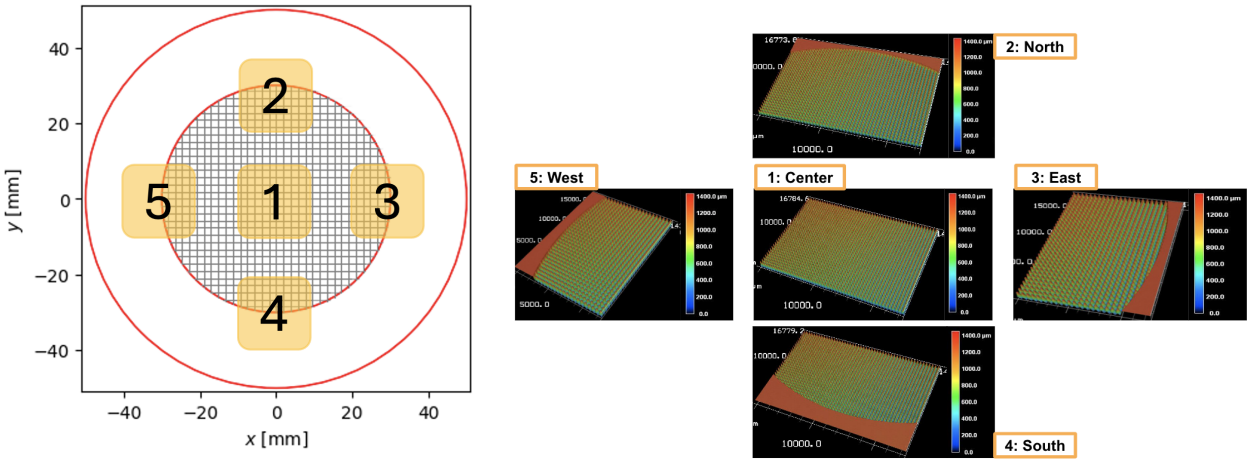

Figure 9. Schematic of sample filter for MF band in a diameter of 60 mm. Confocal microscopy measurements were conducted in five yellow-shaded areas shown on the left. Each measured image is shown on the right.

Table 6. The average of shape parameters of SWS from each five yellow-shaded area in the alumina disk of the diameter of 60 mm. Errors in each row is standard deviation of parameters of all motheyes in each area.

Shape parameters [mm]	1. Center	2. North	3. East	4. South	5. West
Saddle depth x (d_x)	0.90 ± 0.02	0.90 ± 0.02	0.90 ± 0.02	0.90 ± 0.02	0.89 ± 0.02
Saddle depth y (d_y)	0.92 ± 0.02	0.92 ± 0.02	0.94 ± 0.02	0.93 ± 0.02	0.94 ± 0.02
Total depth (d_t)	1.29 ± 0.02	1.28 ± 0.02	1.30 ± 0.02	1.31 ± 0.02	1.30 ± 0.01

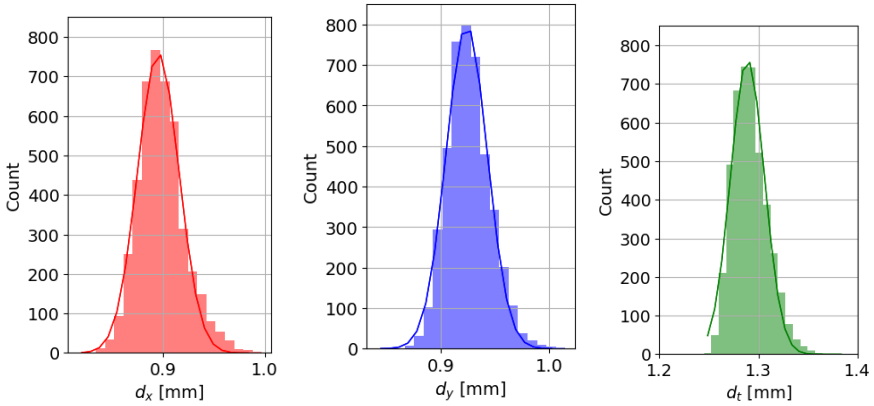

Figure 10. The histograms of extracted geometric parameters from all the selected areas with 4300 pyramids. The means and standard deviations of each fit are listed in Table 7.

Table 7. Mean values and standard deviations of each geometric parameters in mm obtained by fits of 4300 pyramids' histograms.

Shape parameters	MF
Saddle depth x (d_x) [mm]	0.90 ± 0.02
Saddle depth y (d_y) [mm]	0.92 ± 0.02
Total depth (d_t) [mm]	1.29 ± 0.02

Table 8. The volume removal rate at each band.

	LF	MF	HF
VRR [mm^3/min.]	19.8	13.4	3.2

6. CONCLUSIONS

The AR SWS on alumina are designed, fabricated, and evaluated for use as an IR absorptive filter of ground-based CMB polarization experiments. We set the required transmittance of 97% for three typical ground-based millimeter-wave observational bands, LF, MF, and HF. Based on the design using the second-order EMT, we fabricated the 3×3 pyramidal structures and measured their shapes using the confocal microscope. The forecasted transmittance using the RCWA simulator shows the band-averaged transmittance of 0.97 or above in all the bands for the range of the normal incident light to 20 degrees. We also computed the fractional difference of the transmittance between the p-state and the s-state, instrumental polarization, and the band averaged the instrumental polarization as at most $\pm4 \times 10^{-3}$. The fabrication time, quantified as a Volume removal rate (VRR), is computed based on the fabrication time of the 3×3 structures. The VRR for LF, MF, and HF were 19.8, 13.4, and 3.2 mm^3/min, respectively as shown in Table 8. These results make this technology establish the path forward for the laser-ablated SWS AR for an IR filter in future ground-based CMB polarization experiments.

7. ACKNOWLEDGEMENTS

This work was supported by JSPS KAKENHI Grant Number JP23H00107. This study was funded in parts by MEXT Quantum Leap Flagship Program (MEXT Q-LEAP, Grant Number JPMXS0118067246)

REFERENCES

[1] U. Seljak and M. Zaldarriaga, "Signature of gravity waves in the polarization of the microwave background," *Phys. Rev. Lett.* **78**, 2054 (1997).

[2] M. Zaldarriage and U. Seljak, "All-sky analysis of polarization in the microwave background," *Phys. Rev. D* **55**, 1830 (1997).

[3] Hanany, S., Niemack, M., and Page, L., "CMB Telescopes and Optical Systems," *Planets, Stars and Stellar Systems. Volume 1: Telescopes and Instrumentation* (06 2012).

[4] Ade, P. A. R., Pisano, G., Tucker, C., and Weaver, S., "A review of metal mesh filters," in [*Millimeter and Submillimeter Detectors and Instrumentation for Astronomy III*], Zmuidzinas, J., Holland, W. S., Withington, S., and Duncan, W. D., eds., **6275**, 62750U, International Society for Optics and Photonics, SPIE (2006).

[5] Nemoto, T., Sasaki, S., and Hakuraku, Y., "Thermal conductivity of alumina and silicon carbide ceramics at low temperatures," *Cryogenics* **25**(9), 531–532 (1985).

[6] Y. Inoue, T. Matsumura, M. Hazumi, A. T. Lee, T. Okamura, A. Suzuki, T. Tomaru, and H. Yamaguchi, "Cryogenic infrared filter made of alumina for use at millimeter wavelength," *Appl. Opt.* **53**(9), 1727–1733 (2014).

[7] Inoue, Y., Matsumura, T., Hazumi, M., Lee, A. T., Okamura, T., Suzuki, A., Tomaru, T., and Yamaguchi, H., "Cryogenic infrared filter made of alumina for use at millimeter wavelength," *Applied optics* **53**(9), 1727–1733 (2014).

[8] Takaku, R., Wen, Q., Cray, S., Devlin, M., Dicker, S., Hanany, S., Hasebe, T., Iida, T., Katayama, N., Konishi, K., Kuwata-Gonokami, M., Matsumura, T., Mio, N., Sakurai, H., Sakurai, Y., Yamada, R., and Yumoto, J., "Large diameter millimeter-wave low-pass filter made of alumina with laser ablated anti-reflection coating," *Optics express* **29**(25), 41745–41765 (2021).

[9] Schütz, V., Young, K., Matsumura, T., Hanany, S., Koch, J., Suttmann, O., Overmeyer, L., and Wen, Q., "Laser processing of sub-wavelength structures on sapphire and alumina for millimeter wavelength broadband anti-reflection coatings," *Journal of Laser Micro Nanoengineering* **11**, 204–209 (01 2016).

[10] Matsumura, T., Young, K., Wen, Q., Hanany, S., Ishino, H., Inoue, Y., Hazumi, M., Koch, J., Suttman, O., , and Schütz, V., "Millimeter-wave broadband antireflection coatings using laser ablation of subwavelength structures," *Appl. Opt.* **55**, 3502–3509 (May 2016).

[11] Young, K., Wen, Q., Hanany, S., Imada, H., Koch, J., Matsumura, T., Suttmann, O., and Schütz, V., "Broadband millimeter-wave anti-reflection coatings on silicon using pyramidal sub-wavelength structures," *Journal of Applied Physics* **121** (6 2017).

[12] Matsumura, T., Takaku, R., Hanany, S., Imada, H., Ishino, H., Katayama, N., Kobayashi, Y., Komatsu, K., Konishi, K., Kuwata-Gonokami, M., Nakamura, S., Sakurai, H., Sakurai, Y., Wen, Q., Young, K., and Yumoto, J., "Prototype demonstration of the broadband anti-reflection coating on sapphire using a sub-wavelength structure," in [*29th IEEE International Symposium on Space Terahertz Technology, ISSTT 2018*], 54–60 (Jan. 2018). 29th IEEE International Symposium on Space Terahertz Technology, ISSTT 2018 ; Conference date: 26-03-2018 Through 28-03-2018.

[13] Takaku, R., Hanany, S., Imada, H., Ishino, H., Katayama, N., Komatsu, K., Konishi, K., Kuwata-Gonokami, M., Matsumura, T., Mitsuda, K., Sakurai, H., Sakurai, Y., Wen, Q., Yamasaki, N. Y., Young, K., and Yumoto, J., "Broadband, millimeter-wave anti-reflective structures on sapphire ablated with femto-second laser," *Journal of Applied Physics* **128**(22), 225302 (2020).

[14] Takaku, R., Hanany, S., Hoshino, Y., Imada, H., Ishino, H., Katayama, N., Komatsu, K., Konishi, K., Gonokami, M. K., Matsumura, T., Mitsuda, K., Sakurai, H., Sakurai, Y., Wen, Q., Yamasaki, N. Y., Young, K., and Yumoto, J., "Demonstration of anti-reflective structures over a large area for cmb polarization experiments," in [*Millimeter, Submillimeter, and Far-Infrared Detectors and Instrumentation for Astronomy X*], Zmuidzinas, J. and Gao, J.-R., eds., **11453**, 236 – 247, International Society for Optics and Photonics, SPIE (2020).

[15] Wen, Q., Fadeeva, E., Hanany, S., Koch, J., Matsumura, T., Takaku, R., and Young, K., "Picosecond laser ablation of millimeter-wave subwavelength structures on alumina and sapphire," *Optics & Laser Technology* **142**, 107207 (2021).

[16] Takaku, R., Azzoni, S., Ghigna, T., Hasebe, T., Hoang, T. D., Hoshino, Y., Katayama, N., Komatsu, K., Konishi, K., Kuwata-Gonokami, M., Matsumura, T., Sakurai, H., Sakurai, Y., Sugiyama, S., Yamasaki, N. N., and Yumoto, J., "Impact of the effective thickness from anti-reflective sub-wavelength structures in achromatic half-wave plate design," in [*Millimeter, Submillimeter, and Far-Infrared Detectors and Instrumentation for Astronomy XI*], Zmuidzinas, J. and Gao, J.-R., eds., **12190**, 121902K, International Society for Optics and Photonics, SPIE (2022).

[17] Takaku, R., Ghigna, T., Hanany, S., Hoshino, Y., Ishino, H., Katayama, N., Komatsu, K., Konishi, K., Kuwata-Gonokami, M., Matsumura, T., Sakurai, H., Sakurai, Y., Wen, Q., Yamasaki, N. Y., Yumoto, J., and for the LiteBIRD collaboration, "Performance of a 200 mm diameter achromatic hwp with laser-ablated sub-wavelength structures," *Journal of Low Temperature Physics* **211**, 346–356 (Jun 2023).

[18] Ade, P. A. R. et al., "The Latest Constraints on Inflationary B-modes from the BICEP/Keck Telescopes," in [*56th Rencontres de Moriond on Cosmology*], (3 2022).

[19] Austermann, J., Aird, K., Beall, J., Becker, D., Bender, A., Benson, B., Bleem, L., Britton, J., Carlstrom, J., Chang, C., Chiang, H., Cho, H.-m., Crawford, T., Crites, A., Datesman, A., Haan, T., Dobbs, M., George, E., Halverson, N., and Zahn, O., "Sptpol: An instrument for cmb polarization measurements with the south pole telescope," *Proceedings of SPIE - The International Society for Optical Engineering* **8452** (10 2012).

[20] Ghosh, S., Liu, Y., Zhang, L., Li, S., Zhang, J., Wang, J., Dou, J., Chen, J., Delabrouille, J., Remazeilles, M., Feng, C., Hu, B., Huang, Z.-Q., Liu, H., Santos, L., Zhang, P., Zhang, Z., Zhao, W., Li, H., and Zhang, X., "Performance forecasts for the primordial gravitational wave detection pipelines for alicpt-1," *Journal of Cosmology and Astroparticle Physics* **2022**, 063 (oct 2022).

[21] Westbrook, B., Ade, P. A. R., Aguilar, M., Akiba, Y., Arnold, K., Baccigalupi, C., Barron, D., Beck, D., Beckman, S., Bender, A. N., Bianchini, F., Boettger, D., Borrill, J., Chapman, S., Chinone, Y., Coppi, G., Crowley, K., Cukierman, A., de Haan, T., Dünner, R., Dobbs, M., Elleflot, T., Errard, J., Fabbian, G., Feeney, S. M., Feng, C., Fuller, G., Galitzki, N., Gilbert, A., Goeckner-Wald, N., Groh, J., Halverson, N. W., Hamada, T., Hasegawa, M., Hazumi, M., Hill, C. A., Holzapfel, W., Howe, L., Inoue, Y., Jaehnig, G., Jaffe, A., Jeong, O., Kaneko, D., Katayama, N., Keating, B., Keskitalo, R., Kisner, T., Krachmalnicoff, N., Kusaka, A., Le Jeune, M., Lee, A. T., Leon, D., Linder, E., Lowry, L., Madurowicz, A., Mak, D., Matsuda, F., May, A., Miller, N. J., Minami, Y., Montgomery, J., Navaroli, M., Nishino, H., Peloton, J., Pham, A., Piccirillo, L., Plambeck, D., Poletti, D., Puglisi, G., Raum, C., Rebeiz, G., Reichardt, C. L., Richards, P. L., Roberts, H., Ross, C., Rotermund, K. M., Segawa, Y., Sherwin, B., Silva-Feaver, M., Siritanasak, P., Stompor, R., Suzuki, A., Tajima, O., Takakura, S., Takatori, S., Tanabe, D., Tat, R., Teply, G. P.,

Tikhomirov, A., Tomaru, T., Tsai, C., Whitehorn, N., and Zahn, A., "The polarbear-2 and simons array focal plane fabrication status," *Journal of Low Temperature Physics* **193**(5), 758–770 (2018).

[22] Kiuchi, K., Adachi, S., Ali, A. M., Arnold, K., Ashton, P., Austermann, J. E., Bazako, A., Beall, J. A., Chinone, Y., Coppi, G., Crowley, K. D., Crowley, K. T., Dicker, S., Dober, B., Duff, S. M., Fabbian, G., Galitzki, N., Golec, J. E., Gudmundsson, J. E., Harrington, K., Hasegawa, M., Hattori, M., Hill, C. A., Ho, S.-P. P., Hubmayr, J., Johnson, B. R., Kaneko, D., Katayama, N., Keating, B., Kusaka, A., Lashner, J., Lee, A. T., Matsuda, F., McCarrick, H., Murata, M., Nati, F., Nishinomiya, Y., Page, L., Rao, M. S., Reichardt, C. L., Sakaguri, K., Sakurai, Y., Sibert, J., Spisak, J., Tajima, O., Teply, G. P., Terasaki, T., Tsan, T., Walker, S., Wollack, E. J., Xu, Z., Yamada, K., Zannoni, M., and Zhu, N., "Simons Observatory Small Aperture Telescope overview," in [*Ground-based and Airborne Telescopes VIII*], Marshall, H. K., Spyromilio, J., and Usuda, T., eds., **11445**, 114457L, International Society for Optics and Photonics, SPIE (2020).

[23] Barron, D. R., Bender, A. N., Birdwell, I. E., Carlstrom, J. E., Delabrouille, J., Guns, S., Kovac, J., Lawrence, C. R., Paine, S., and Whitehorn, N., "Review of radio frequency interference and potential impacts on the cmb-s4 cosmic microwave background survey," (2022).

[24] Zhu, N., Bhandarkar, T., Coppi, G., Kofman, A. M., Orlowski-Scherer, J. L., Xu, Z., Adachi, S., Ade, P., Aiola, S., Austermann, J., Bazarko, A. O., Beall, J. A., Bhimani, S., Bond, J. R., Chesmore, G. E., Choi, S. K., Connors, J., Cothard, N. F., Devlin, M., Dicker, S., Dober, B., Duell, C. J., Duff, S. M., Dünner, R., Fabbian, G., Galitzki, N., Gallardo, P. A., Golec, J. E., Haridas, S. K., Harrington, K., Healy, E., Ho, S.-P. P., Huber, Z. B., Hubmayr, J., Iuliano, J., Johnson, B. R., Keating, B., Kiuchi, K., Koopman, B. J., Lashner, J., Lee, A. T., Li, Y., Limon, M., Link, M., Lucas, T. J., McCarrick, H., Moore, J., Nati, F., Newburgh, L. B., Niemack, M. D., Pierpaoli, E., Randall, M. J., Sarmiento, K. P., Saunders, L. J., Seibert, J., Sierra, C., Sonka, R., Spisak, J., Sutariya, S., Tajima, O., Teply, G. P., Thornton, R. J., Tsan, T., Tucker, C., Ullom, J., Vavagiakis, E. M., Vissers, M. R., Walker, S., Westbrook, B., Wollack, E. J., and Zannoni, M., "The simons observatory large aperture telescope receiver," *The Astrophysical Journal Supplement Series* **256**, 23 (sep 2021).

[25] Errard, J., Ade, P. A. R., Akiba, Y., Arnold, K., Atlas, M., Baccigalupi, C., Barron, D., Boettger, D., Borrill, J., Chapman, S., Chinone, Y., Cukierman, A., Delabrouille, J., Dobbs, M., Ducout, A., Elleflot, T., Fabbian, G., Feng, C., Feeney, S., Gilbert, A., Goeckner-Wald, N., Halverson, N. W., Hasegawa, M., Hattori, K., Hazumi, M., Hill, C., Holzapfel, W. L., Hori, Y., Inoue, Y., Jaehnig, G. C., Jaffe, A. H., Jeong, O., Katayama, N., Kaufman, J., Keating, B., Kermish, Z., Keskitalo, R., Kisner, T., Jeune, M. L., Lee, A. T., Leitch, E. M., Leon, D., Linder, E., Matsuda, F., Matsumura, T., Miller, N. J., Myers, M. J., Navaroli, M., Nishino, H., Okamura, T., Paar, H., Peloton, J., Poletti, D., Puglisi, G., Rebeiz, G., Reichardt, C. L., Richards, P. L., Ross, C., Rotermund, K. M., Schenck, D. E., Sherwin, B. D., Siritanasak, P., Smecher, G., Stebor, N., Steinbach, B., Stompor, R., Suzuki, A., Tajima, O., Takakura, S., Tikhomirov, A., Tomaru, T., Whitehorn, N., Wilson, B., Yadav, A., and Zahn, O., "Modeling atmospheric emission for cmb ground-based observations," *The Astrophysical Journal* **809**, 63 (aug 2015).

[26] "Kenji Kiuchi, Shunsuke Adachi, Aamir M. Ali, Kam Arnold, Peter Ashton, Jason E. Austermann, Andrew Bazako, James A. Beall, Yuji Chinone, Gabriele Coppi, Kevin D. Crowley, Kevin T. Crowley, Simon Dicker, Bradley Dober, Shannon M. Duff, Giulio Fabbian, Nicholas Galitzki, Joseph E. Golec, Jon E. Gudmundsson, Kathleen Harrington, Masaya Hasegawa, Makoto Hattori, Charles A. Hill, Shuay-Pwu Patty Ho, Johannes Hubmayr, Bradley R. Johnson, Daisuke Kaneko, Nobuhiko Katayama, Brian Keating, Akito Kusaka, Jack Lashner, Adrian T. Lee, Frederick Matsuda, Heather McCarrick, Masaaki Murata, Federico Nati, Yume Nishinomiya, Lyman Page, Mayuri Sathyanarayana Rao, Christian L. Reichardt, Kana Sakaguri, Yuki Sakurai, Joseph Sibert, Jacob Spisak, Osamu Tajima, Grant P. Teply, Tomoki Terasaki, Tran Tsan, Samantha Walker, Edward J. Wollack, Zhilei Xu, Kyohei Yamada, Mario Zannoni, Ningfeng Zhu", "Simons observatory small aperture telescope overview," in [*2020 SPIE*], Heather K. Marshall, Jason Spyromilio, Tomonori Usuda, ed., *Proc. SPIE* **11445**, 1–8 (2020).

[27] Klopfenstein, R. W., "A transmission line taper of improved design," in [*Proceedings of the IRE*], **44**(1), 31 – 35, IEEE (1956).

[28] Hecht, E., [*OPTICS FIFTH EDITION*], Pearson (2017).

[29] Takaku, R., Hanany, S., Imada, H., Ishino, H., Katayama, N., Komatsu, K., Konishi, K., Kuwata-Gonokami, M., Matsumura, T., Mitsuda, K., Sakurai, H., Sakurai, Y., Wen, Q., Yamasaki, N. Y., Young, K., and Yumoto, J., "Broadband, millimeter-wave anti-reflective structures on sapphire ablated with femto-second laser," *Journal of Applied Physics* **128**(22), 225302 (2020).